

## **Optimizing lateral homogeneity of ion-induced surface modifications of non-planar dielectric polyethylene components employing ion fluence simulations and optical measurements of the sp<sup>2</sup>-dependent reflectivity**

**Jochen Taiber, Sascha Buchegger, Bernd Stritzker, Achim Wixforth, Christoph Westerhausen**

### **Angaben zur Veröffentlichung / Publication details:**

Taiber, Jochen, Sascha Buchegger, Bernd Stritzker, Achim Wixforth, and Christoph Westerhausen. 2018. "Optimizing lateral homogeneity of ion-induced surface modifications of non-planar dielectric polyethylene components employing ion fluence simulations and optical measurements of the sp<sup>2</sup>-dependent reflectivity." Nuclear Instruments and Methods in Physics Research Section B: Beam Interactions with Materials and Atoms 433: 98-105.  
<https://doi.org/10.1016/j.nimb.2018.07.034>.

1 **Optimizing lateral homogeneity of ion-induced surface modifications of non-**  
2 **planar dielectric polyethylene components employing ion fluence simulations**  
3 **and optical measurements of the sp<sup>2</sup>-dependent reflectivity**

4  
5 Jochen Taiber<sup>1</sup>, Sascha Buchegger<sup>1</sup>, Bernd Stritzker<sup>1</sup>, Achim Wixforth<sup>1,2,3</sup>, and Christoph  
6 Westerhausen<sup>1,2,3</sup>  
7

8 <sup>1</sup> Chair for Experimental Physics 1, University of Augsburg, Augsburg 86159, Germany

9 <sup>2</sup> Center for NanoScience (CeNS), Ludwig-Maximilians-Universität Munich, 80799  
10 Munich, Germany

11 <sup>3</sup> Augsburg Center for Innovative Technologies (ACIT), Augsburg 86159, Germany

12 \* Correspondence: christoph.westerhausen@gmail.com; Tel.: +49-821-598-3311  
13

14  
15  
16 ***Abstract* — An approach to enhance the durability of artificial joint replacements is to**  
17 **modify the surface of their polymeric bearing material to diamond-like carbon (DLC) by**  
18 **ion-induced polymer-to-DLC-transformation in a plasma-immersion ion implantation**  
19 **process. Due to the dielectric character of the polymer and thus the impossibility of direct**  
20 **application of high voltage pulses to the component, this process requires an additional**  
21 **accelerator electrode above the surface. We here present two useful tools to optimize the**  
22 **geometry of such electrodes. First, we simulate the ions' trajectories for various electrode**  
23 **geometries and receive the resulting fluence distribution across the surface of the treated**  
24 **part. Second, we introduce a novel optical method to determine non-destructively the local**  
25 **ratio of sp<sup>2</sup> hybridized carbon atoms and thus the locally implanted fluence utilizing**  
26 **changes in reflectivity. Combining both tools, we here optimize, by way of example, the**  
27 **geometry of a grid electrode to obtain a homogeneous DLC-modification of a typical hip**  
28 **replacement inlay.**  
29  
30

## 31 **1. Introduction**

32 Representing the sixth most frequent surgery in Germany in 2016, the implantation of a hip  
33 total endoprosthesis was performed more than 230,000 times [1]. Considering the demographic  
34 change - the share of citizens of the overall population at the age of 65 and older will increase  
35 from 21% in 2013 to 33% in 2060 [2] - and the average age for primary total hip joint  
36 replacements (currently 69.7 years [3]), the interest in increasing the life span of an artificial  
37 joint replacement is clearly visible. The service life in today's joint replacement amounts to 15  
38 to 20 years which explains the quantity of about 47,000 revision surgeries (hip + knee) in 2014  
39 in Germany [4]. Aseptic loosening accounts for more than two thirds of all failing issues and is  
40 mainly caused by wear debris increasing the activity of macrophages and osteoclasts and ending  
41 up in enhanced osteolysis and thereby loosening of the implant [5].

42  
43 Considering the amount of wear particles, a major step has been taken by using highly cross-  
44 linked polyethylene as inlay material in combination with a ceramic joint head [6–8]. Further  
45 progress could be possible with the application of diamond-like carbon (DLC); an amorphous  
46 modification with a significant portion of  $sp^3$  hybridized carbon atoms (at least 10%) showing  
47 high hardness, excellent biocompatibility and low surface roughness [9,10].

48  
49 Therefore, DLC coatings are used in a broad range of industrial applications: Especially its  
50 outstanding tribological properties qualify it for bearings, sliding surfaces and protective  
51 coatings, e.g. in the automotive industry, for magnetic storage media or, as mentioned, in a  
52 medical context [11]. In principal, the metastable DLC is prepared under ion bombardment of  
53 the growing film [12]. The desired film composition and thus its properties strongly depend on  
54 the deposition method which can mainly be categorized in PVD (physical vapor deposition)  
55 and PECVD (plasma-enhanced chemical vapor deposition) techniques. Hydrogenated forms of  
56 DLC (a-C:H) can be produced in a PECVD process in which the vapour deposition occurs due

57 to chemical reactions on the substrate. The required energy is provided by a plasma which thus  
58 allows much lower process temperatures compared to common CVD [12–14]. In contrast,  
59 hydrogen free amorphous carbon (a-C) and tetrahedral amorphous carbon (ta-C) films result  
60 from PVD where a carbon containing material is evaporated and the carbon ions are condensed  
61 to the substrate's surface. Common PVD processes are magnetron sputtering (often used in  
62 industrial applications), pulsed laser deposition or vacuum arc evaporation [10,15–18].

63

64 Another appropriate way of realizing diamond-like properties is the ion bombardment of a  
65 polymeric base material leading to densification, hydrogen loss and cross-linking of the carbon  
66 network and finally resulting in a DLC modification of the surface layer up to a depth of about  
67 300 nm [19,20]. Compared to common coatings, the risk of delamination is strongly reduced  
68 due to the decreased layer tension as result of the range distribution of the ions and thus a  
69 gradient in hardness and density [21,22]. A further benefit is the easy integration of antibacterial  
70 properties by implanting metal nanoparticles [23].

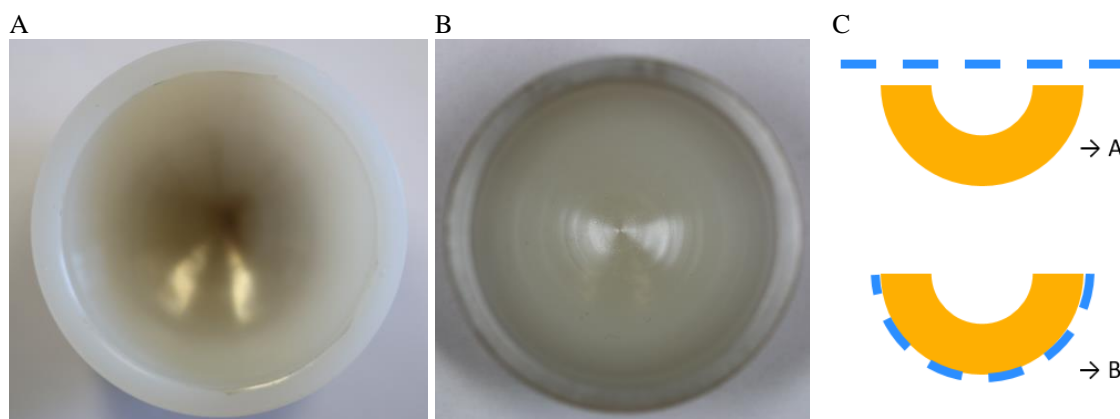


FIG 1: Modification of non-planar samples A) Inhomogeneous surface modification using a flat top-side grid-electrode B) Homogeneous modification using a backside-electrode. C) Illustration of flat top and curved backside electrode.

71

72 Ion implantation in electrically conducting objects using Plasma Immersion Ion Implantation  
73 is easily possible [24]. On the contrary, surface modifications of an insulating polymer can  
74 either be performed by using an additional cathode above the surface or at the sample's  
75 backside. This can be realized in a simple way for planar samples. However, complex-shaped

76 objects require greater effort, especially if the use of a back-side electrode is not possible due  
77 to a variation of the sample thicknesses resulting in a variation of the effective electrical field.  
78 Because of the dependence on the orientation of the surface according to the moving direction  
79 of the accelerated ions, DLC modification becomes inhomogeneous for non-planar components  
80 in the case of a flat grid cathode (see fig. 1 a)). Therefore, the geometry of the electrode has to  
81 be optimized for each specific sample geometry.

82

83 To do so, we simulated the ions' trajectories using different geometries of the grid electrode to  
84 gain the implanted ion density on the surface of the implant. Using the developed simulation,  
85 we optimized the electrode shape for homogeneous surface modification of a hip inlay. As a  
86 second step, we introduced a novel optical method to determine non-destructively and space-  
87 resolved the ion fluence locally implanted into complex shaped surfaces. Based on the  
88 measurement of the local reflectivity which varies according to the local ratio of sp<sup>2</sup> hybridized  
89 carbon atoms, this method allows to measure the implanted ion fluence and thus gives  
90 information about the homogeneity of the surface modification. Combining simulation and  
91 optical examination, it is possible to optimize the geometry of the grid electrode for  
92 homogeneous modification adapted to the shape of the component.

93

## 94 **2. Materials and methods**

95

### 96 **DLC**

97 As primary material we used a highly cross-linked Ultra High Molecular Weight Polyethylene  
98 (UHMWPE) which is vitamin E stabilized (Vitelene<sup>®</sup>, Aesculap AG, Germany) [25,26] and  
99 has a molecular mass of about 5000 kg/mol before irradiation [27].

100 We transformed the surface of the polymer to DLC by implanting ions in a plasma immersion  
101 ion implantation step. Due to cross-linking, densification and a rearrangement of bonds, this

102 process leads to the formation of a diamond-like carbon surface. For this process, we used a gas  
103 mixture of 20% Argon and 80% Hydrogen at a pressure of  $p = 5 \cdot 10^{-3}$  mbar. We applied  $P_m =$   
104 800 W of microwave power ( $f = 2.45$  GHz) to generate the plasma in an electron cyclotron  
105 resonance (ECR) plasma source. The ions of the plasma were accelerated towards the surface  
106 by applying a pulsed high voltage of  $V_p = 20$  kV with a repetition rate of  $f_R = 20$  Hz and a pulse  
107 width of  $\tau = 5$   $\mu$ s to the electrode grid. Due to the range distribution of the impinging ions, the  
108 result is an about 300 nm thick surface near region of DLC with a gradient in hardness, density  
109 and diamond-like properties. This gradient reduces the internal stress and could be of great  
110 advantage for the adhesion of the DLC-surface and could therefore improve the long-time  
111 stability of the surface.

112

113

#### 114 **Simulation**

115 To evaluate space-resolved the implanted fluence on the sample surface, we simulated the  
116 trajectories of the ions which are extracted from the plasma boundary sheath and accelerated  
117 towards the grid electrode, passing it and finally hitting the target's surface, as illustrated in  
118 fig. 2.

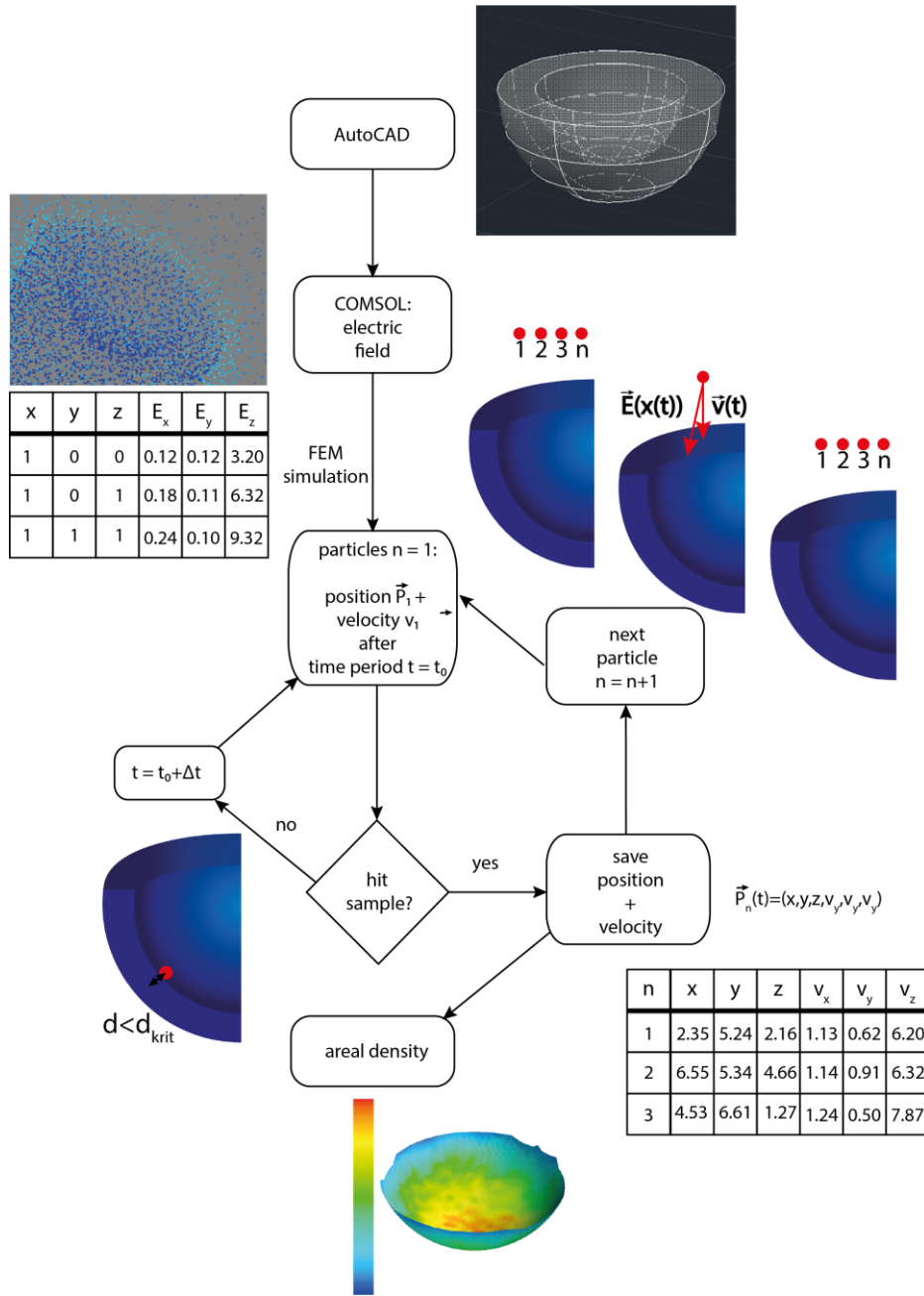


FIG 2: Schematic illustration of the simulation.

119

120 As first step, we modelled all components (inlay, grid electrode etc.) by using a common 3D

121 computer-aided design software (Autodesk AutoCAD<sup>®</sup> 2017) which also makes it possible to

122 integrate existing 3D models, for example a commercially available hip inlay. The plasma was

123 simulated by an arrangement of positive charged particles with a median distance of 72 mm to

124 the electrode. The median distance was estimated using Child's Law, which shows that the

125 plasma sheet expands from 18 mm to 132 mm during a 5  $\mu$ s lasting high voltage pulse. Because

126 of the low impact of this distance on the ion trajectory, we simply assumed an intermediary  
127 distance of 72 mm. According to the experimental setup the mesh size of the grid cathode varied  
128 from 0.16 mm to 1.5 mm. However, above a distinct distance between electrode and sample,  
129 the grid characteristic of the anode can be neglected and the electrode can be replaced by a  
130 massive body which is penetrable by ions (see 3. *Results: Grid shading*).

131

132 By utilizing a finite element tool (Comsol Multiphysics® 5.2.0.220 with AC/DC (electrostatics)  
133 and CAD Import module) we then simulated the electric field of the arrangement. To keep the  
134 computing time within an acceptable range, a physics-controlled mesh was used with higher  
135 point density on the sample to improve accuracy. The electric field as well as the geometries of  
136 the electrode and the sample were subsequently exported as a point cloud to a python script.

137

138 As first step of the script, a starting configuration was generated distributing the particles  
139 equally across the plasma boundary sheet (spherical or circular). The particle state at a point in  
140 time is defined as a vector with six components describing the position and the velocity of the  
141 particle:  $\vec{p}_n = (x, y, z, v_x, v_y, v_z)$ . For each particle and each time step, the nearest point of the  
142 electric field was identified by determining the distances to all other points. By means of this  
143 electric field value, the movement of the considered particle was calculated using suitable  
144 parameters (e.g. the corresponding ion mass). This was repeated as long as the distance between  
145 the particle and the electrode or sample has not fallen below the before defined minimum  
146 distance.

147

148 The evaluation of the results was implemented in two ways. For grasping all important  
149 information at a glance, a graphical approach was used performing a Delaunay triangulation of  
150 the sample's surface and assigning each triangle a distinct colour according to the calculated  
151 particle density at the corresponding position. For a more quantitative evaluation, we used two

152 custom python analysis scripts to plot the particle density against its position on the sample's  
153 surface. As per default the script averages over either a rectangular interval (planar sample) or  
154 a 5°-segment of a spherical zone, depending on the geometry of the sample.

155

### 156 **Optical measurement: ion-induced colour change**

157 The optical measurement of the DLC modification is based on determining the reflectivity of  
158 the sample at a distinct wavelength interval. As can be seen in fig. 4 a), the higher the implanted  
159 fluence, the darker the surface appears. Furthermore, a yellowish tint occurs which transforms  
160 into a bronze colour at high fluences accompanied by an increasing metallic gloss [28]. The  
161 reason for this behaviour can be found in the bonding structure of the material: it is well known  
162 that the energy differences between molecular vibrations and rotations in usual polymers are  
163 too small and the differences between different electron states are too large for excitation within  
164 the visible range [29]. But the situation is different if there are delocalized  $\pi$  electrons. In this  
165 case, the energy gap between the highest occupied and the lowest unoccupied molecular orbital  
166 is decreasing which lowers the energy threshold and leads to an absorption of light with a larger  
167 wavelength.

168

169 In the polyethylene starting material, a large fraction of carbon atoms is  $sp^3$  hybridized and  
170 bound to further carbon or hydrogen atoms via  $\sigma$  bonds. The DLC transformation increases the  
171 percentage of  $sp^2$  hybridized carbon atoms resulting in a larger amount of  $\pi$  electrons. Inter alia,  
172 being arranged in olefinic or even forming entire  $sp^2$  clusters, the delocalization of these  $\pi$   
173 electrons becomes larger and larger [10,21,30]. Thus, the energy threshold decreases which  
174 allows absorption of blue light leading to the described yellowish tint of the sample and its  
175 darker appearance. According to the investigations of Schwarz-Selinger et al. [30], the  
176 compaction of the material during DLC transformation induces an increase in the refractive  
177 index. Dowling et al. [31] showed that this results in a higher extinction coefficient and thus in

178 a higher reflection which explains the metal gloss of the DLC layer. We assume that, similar to  
179 the high mobility of the conduction electrons in metals, the delocalization of the  $\pi$  electrons in  
180 DLC layers hence plays the key role for the gloss. This description is in accordance to previous  
181 publications [32–34], but should not be further elaborated as this study focusses on employing  
182 this optical phenomenon to evaluate the implanted fluence.

183

### 184 **Optical measurement: setup**

185 To investigate complex-shaped objects, a flexible setup with high reproducibility is necessary.  
186 Thus, we chose a reflectivity measurement via optical fibres to enable examinations in any  
187 orientation without having to take care of the illumination of the sample. As can be seen in fig.  
188 3, the light from the light source (LED or Xenon lamp) was coupled into a reflection probe

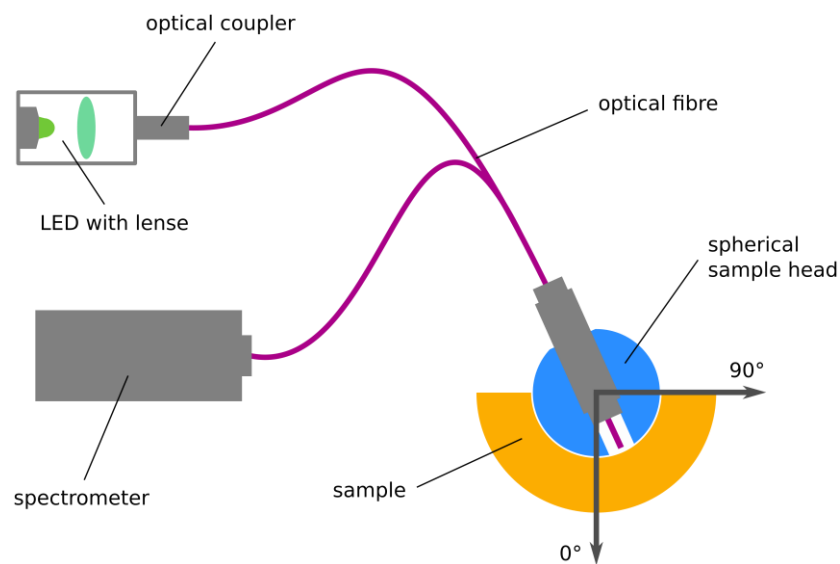


FIG 3: Illustration of the optical measurement of the local reflectivity as a measure for the local applied fluence.

189 (Thorlabs RP22) which was connected to a sample head, here in a spherical shape made of a  
190 ceramic femoral head. Thus, it was possible to keep the distance between the end of the fibre  
191 and the surface of the sample very constant which is indispensable for accurate measurements.  
192 The intensity of the reflected radiation was detected by a spectrometer (Ocean Optics QE65000)  
193 or a power meter (Thorlabs PM100D / S150C).

194

195 **3. Results**

196 **Spectral Range**

197 For choosing an appropriate spectral range, we first recorded spectra between 400 nm and 1000  
198 nm using five different standard samples (CNC-milled UHMWPE wafers having a diameter of  
199 10 mm), treated with fluences of  $2 \cdot 10^{17} \text{ cm}^{-2}$ ,  $1 \cdot 10^{17} \text{ cm}^{-2}$ ,  $5 \cdot 10^{16} \text{ cm}^{-2}$ ,  $1 \cdot 10^{16} \text{ cm}^{-2}$  and  $0 \text{ cm}^{-2}$   
200 (no treatment). The resulting values were normalized using the values of light reflected by a  
201 mirror to eliminate the influence of the emission and are shown in fig. 4. By plotting the  
202 reflectance as function of the fluence for a distinct wavelength, a calibration curve can be  
203 obtained and fitted according to the equation  $y = A \cdot e^{-\frac{x}{\tau}} + y_0$ . This way, it is possible to  
204 directly translate the measured intensity data into fluence values.

205

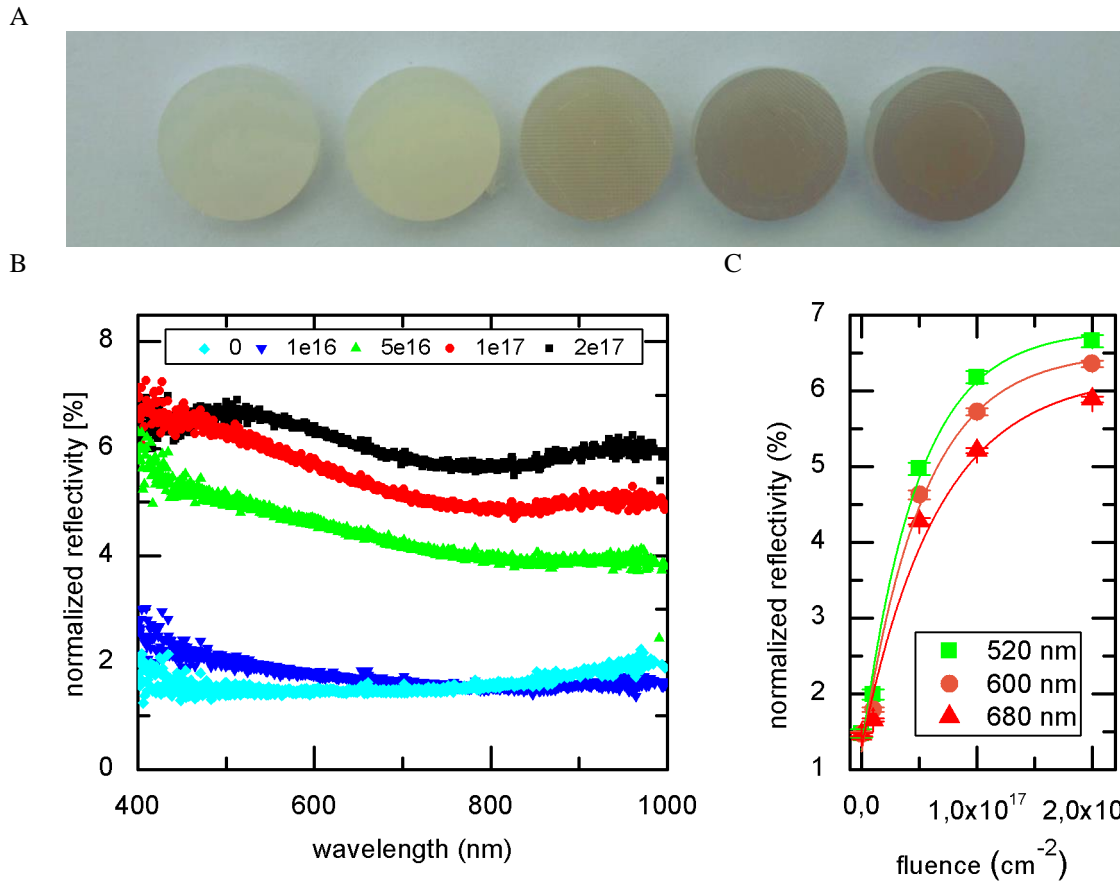


FIG 4: A) A colour change with increasing fluence is obvious. B) Reflectivity as function of wavelength for different fluences in units of  $\text{cm}^{-2}$ . C) Reflectivity as function of fluence for selected wave lengths fitted to exponential functions  $y_{520\text{nm}} = -5.6\% \cdot e^{-\frac{x}{4.8 \cdot 10^{16}}} + 6.8\%$ ,  $y_{600\text{nm}} = -5.3\% \cdot e^{-\frac{x}{5.3 \cdot 10^{16}}} + 6.5\%$  and  $y_{680\text{nm}} = -4.8\% \cdot e^{-\frac{x}{5.5 \cdot 10^{16}}} + 6.0\%$ .

206

207 The reflectivity increases with increasing fluence until a saturation value is reached.

208 Furthermore, it also slightly increases with decreasing wavelength which is consistent with the

209 theoretical predictions. In the range between  $\lambda = 520 \text{ nm}$  and  $\lambda = 700 \text{ nm}$  conclusions about the

210 fluence have the highest significance. Since in general the highest contrast can be observed at

211  $\lambda = 520 \text{ nm}$ , we used a green high-power LED with a wavelength of  $\lambda = 518 \text{ nm}$  for our

212 measurements. To optimize the measurements for the high fluence regime higher wavelengths

213 e.g.  $\lambda = 900 \text{ nm}$  can be chosen.

214

215 **Grid shading**

216 To demonstrate the performance of the described optical measurement method, we modified  
217 cylindrical UHMWPE samples (thickness 2 mm, diameter 1mm) using a coarse grid (mesh size  
218  $w = 1.5$  mm, wire diameter  $d_w = 0.7$  mm) which was placed at an adjustable distance  $d$  to the  
219 sample's surface.

220 The corresponding samples are shown in fig. 5 b): at the bright positions no ions reached the  
221 sample, whereas in the dark areas a DLC modification occurred. For the optical measurements  
222 we used a modified experimental setup where the fibre is fixed on a microscope stage and can  
223 be moved precisely in steps of 0.5 mm along the X and Y axes in constant distance of 0.5 mm  
224 to the surface. Figs. 5 c)-f) show the measured averaged fluence depending on the position on  
225 the sample in X direction. Obviously, there is a high level of agreement between the results  
226 determined by measuring the reflectance and the optical appearance of the samples shown in  
227 the photography.

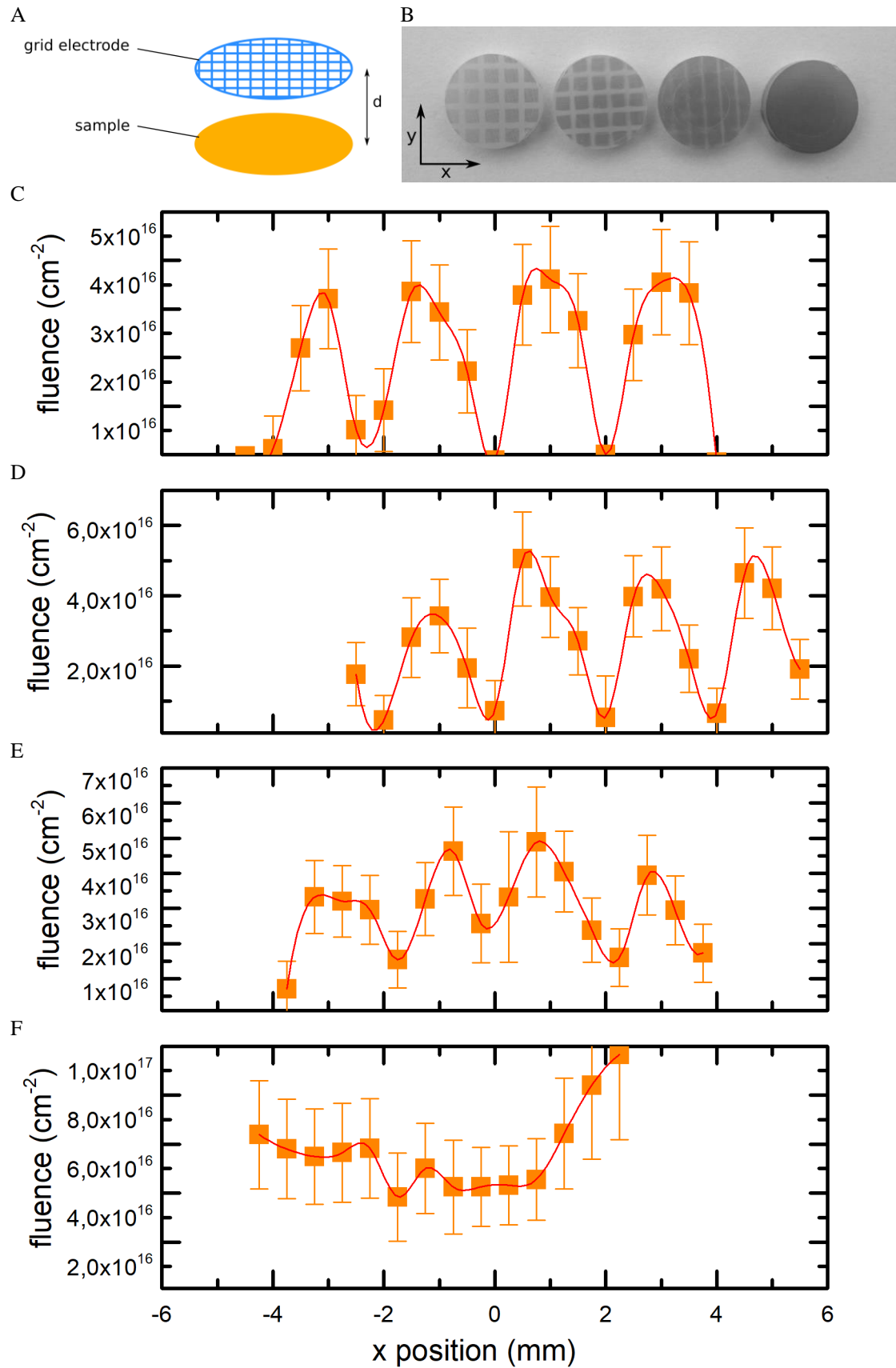


FIG 5: A) Illustration of the sample and mesh geometry B) Shadowing of the mesh during implantation for different fluences C)-F) Optical measurement of the implanted fluence

230 Measuring the reflectivity shows a width of the shadowing between 0.5 and 1 mm for the  
 231 sample which has been modified with a sample to grid distance of 0 mm. This corresponds to  
 232 the wire diameter and to the optical appearance of the sample shown in fig. 5 b). With increasing  
 233 gap between sample and electrode, the resulting width of the shadow becomes gradually thinner  
 234 and blurs until it nearly disappears at a distance of 50 mm. Above that distance, we therefore  
 235 get a homogeneous surface modification with a constant fluence all over the surface of the  
 236 sample. These results prove that the optical measurement of the sample's reflectivity is in  
 237 accordance to the appearance of the sample and corresponds to the geometry of the sample and  
 238 the electrode grid used in the experimental setup.

239 The simulation data (in fig. 6 shown for the 10-mm-case; in each case 10,000 particles  
 240 simulated) also strongly support these findings. The peak positions are almost identical whereas  
 241 the uncertainties are relatively high (about  $2 \cdot 10^{16} \text{ cm}^{-2}$ ) in the measurement.

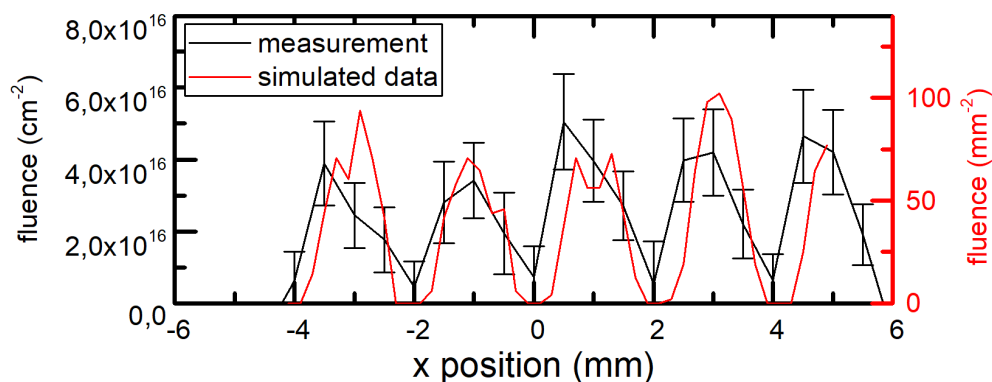


FIG 6: Simulated and measured implantation fluence for  $d=10 \text{ mm}$ .

242 The latter could be explained by two influences: first, the accuracy of the optical measurements  
 243 strongly depends on the smoothness of the surface. In our case we used samples with a  
 244 comparatively rough surface ( $R_A = 0.9 \mu\text{m}$ ) which corresponds to a typical roughness of  
 245 polymer sliding surfaces in orthopaedic joint replacements, additionally affected by scratches  
 246 from the CNC milling process. Second, the calibration curve (reflectivity as function of fluence)  
 247 is significantly flatter for high fluences than for low ones. Consequently, measurements are  
 248 much more sensitive in the low fluence regime. Nevertheless, the comparison of the simulated  
 249 ion distribution and the measured fluence demonstrates that both methods are first in high

250 accordance with each other and second in high accordance to the used experimental setup. This  
251 shows that we are able to cost-efficiently simulate the homogeneity of the treatment for any  
252 setup of sample and electrode. Furthermore, we can non-destructively measure the implanted  
253 fluence and therefore the homogeneity of the treatment.

254 Because of this coarse grid, primarily used for demonstration of the accuracy of the simulation  
255 and the optical measurement method, there is no relevant shading at relatively high distances  
256 above 50 mm between grid and sample. For the treatment of artificial joint components with  
257 plasma immersion ion implantation it is, however, more appropriate to use a finer grid  
258 electrode. Transferred to that which we used in the following experiments (mesh size of 0.16  
259 mm, wire diameter of 0.112 mm), an electrode sample of about 5 mm is sufficient to prevent  
260 shading. To limit the required calculation time, we thus renounced modelling the full grid in  
261 the following simulations and replaced it by solid sheets that are assumed transparent for  
262 incoming particles.

263

264 **Optimization of the implanted ion distribution for a joint inlay**

265 In the following, we demonstrate, by way of example, the optimization of a hip inlay used as  
266 one part of the sliding surface in artificial joint replacements. The aim here is to homogeneously  
267 modify the component's surface to DLC and to optimize the geometry of the grid electrode for  
268 this purpose. Fig. 7 a) illustrates the use of a flat grid electrode above the hemispherical hip  
269 inlay which leads to strongly inhomogeneous results (Fig. 7b). Most of the ions are implanted  
270 in the centre where the surface is perpendicular to the moving direction of the particles and  
271 almost no implantation occurs on the outer area of the hip inlay. We therefore deformed the  
272 grid electrode in a way that it is equally spaced to the sample's surface. As can be seen from

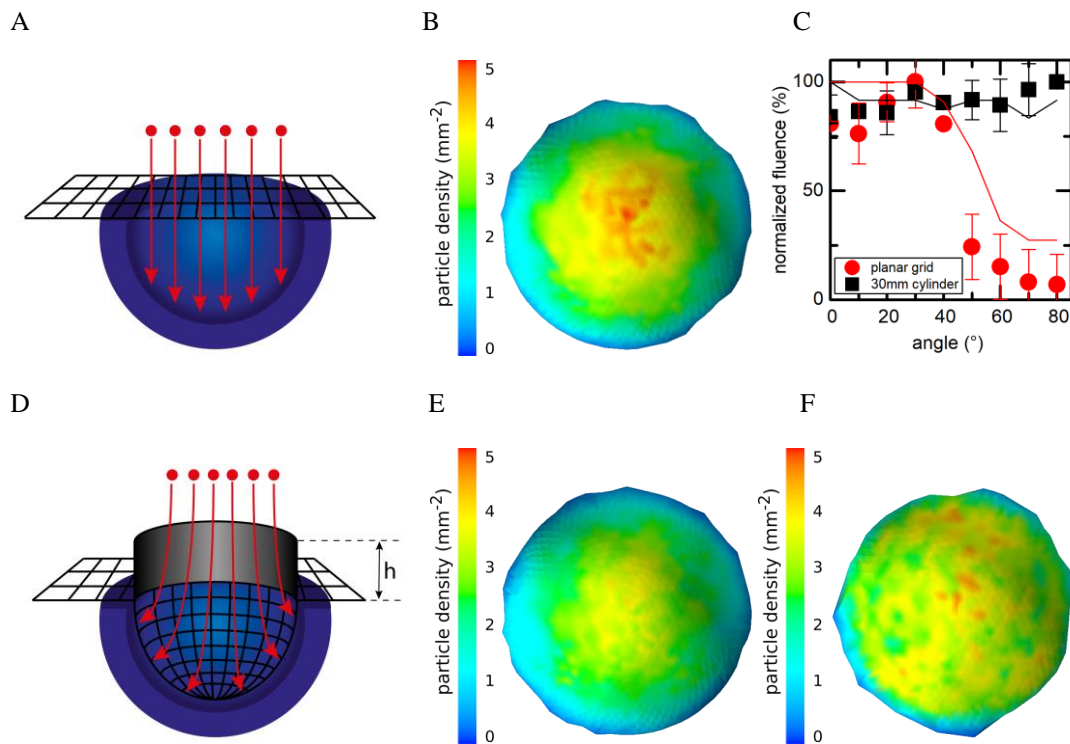


FIG 7: A) Illustration of the planar grid B) Simulated particle density after implantation C) Comparison of Simulation and measurement D) Illustration of a grid with additional cylinder of variable height E) Simulation of cylinder height  $h=0$  mm and F)  $h=30$  mm.

273 fig. 7 e), this electrode geometry shows almost the same result with a high fluence to the centre  
274 of the sample and almost no fluence on the outer area of the sample. To achieve ion implantation  
275 to the outer area of the hip inlay, a force directed radially outwards is necessary to deflect the  
276 ions. To get a radial force, we added a metallic hollow cylinder to the top of the mesh as shown

277 in fig. 7 d). In the simulation, 21,600 ions are simulated and the height of the cylinder is varied  
278 from 0 mm (no cylinder) to 40 mm in steps of 5 mm (see Supporting Information). As shown  
279 in fig. 7 f), the fluence becomes most evenly distributed for a cylinder height of 30 mm which  
280 was experimentally verified by producing and measuring corresponding samples (see fig. 7 c)).  
281 This result is also consistent regarding the total number of particles hitting the sample's surface  
282 in the simulation: If the cylinder is higher than 30 mm, some particles are accelerated towards  
283 the shell of the cylinder and therefore the total number of particles hitting the sample's surface  
284 decreases for higher cylinders. If the cylinder is lower, the treatment becomes inhomogeneous.  
285 Therefore, the optimal height of the cylinder is 30 mm, leading to relatively homogeneous  
286 results.

287

288 Based on the above shown high correlation of simulations and experimental data, we simulated  
289 and analysed a spherical electrode structure as shown in fig. 8: a hemispherical grid is  
290 spherically continued and fixed to a thin mount. The idea is that the plasma boundary sheet can  
291 spread undisturbed around the electrode so that the trajectories of the ions run perpendicular to  
292 the surface. Considering the simulation results (see fig. 8; 22,000 particles simulated), this setup  
293 results in a highly homogenous DLC modification over the whole relevant surface of the joint  
294 inlay, differences in fluence are negligibly small. Therefore, we propose the use of a spherical  
295 grid electrode to homogeneously modify the surface of a UHMWPE hip inlay to DLC.

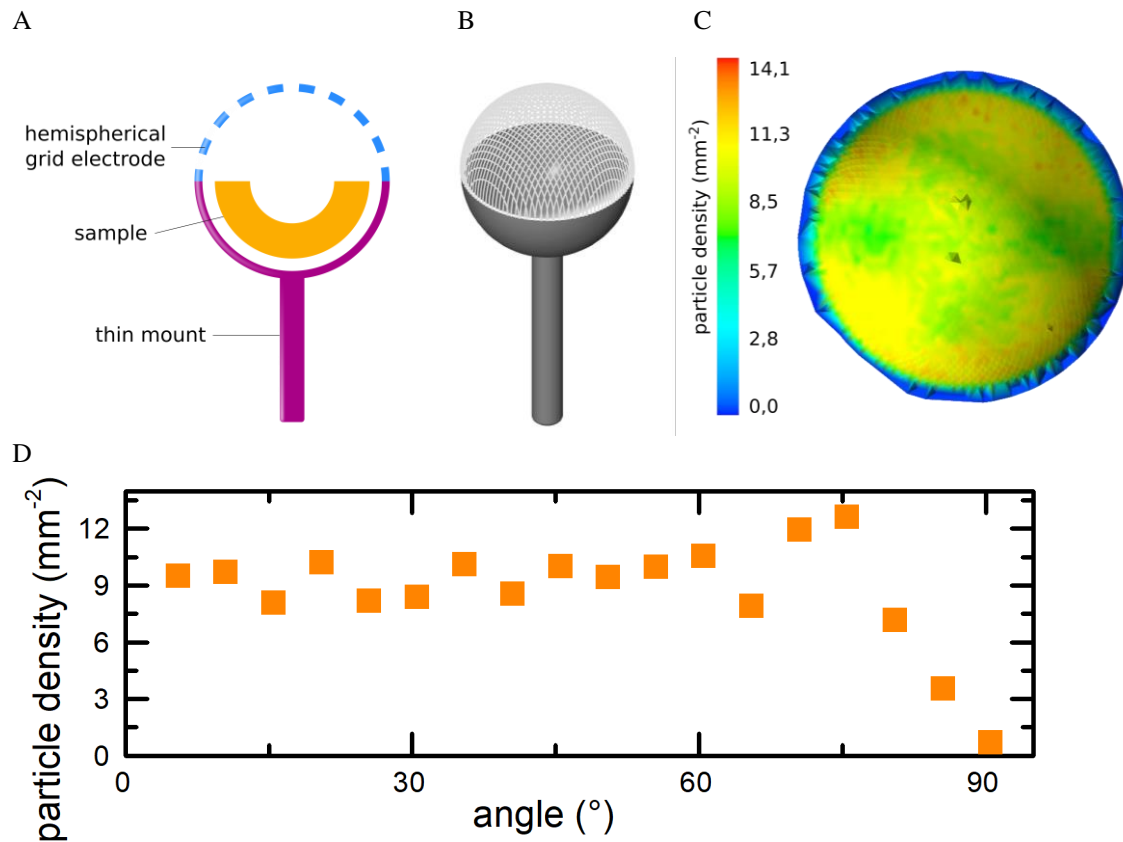


FIG 8: A)+B) Illustration of the hemispherical electrode setup C)+D) Simulation using a hemispherical electrode.

296

#### 297 4. Conclusion

298 Considering complex-shaped dielectric parts for the homogeneous modification to diamond-  
 299 like carbon, it is not possible to apply a high voltage directly. Thus, it is necessary to design a  
 300 complex-shaped electrode which is placed above the surface. We therefore deliver two tools to  
 301 optimize such grid electrodes.

302 First, we implemented a three-dimensional simulation process based on finite element analysis  
 303 software and python scripts to calculate and visualize the ion density on the sample's surface  
 304 which is a measure for DLC modification. The simple integration of diverse 3D CAD models  
 305 enables a fast evaluation of multiple electrode geometries without the need of physically  
 306 producing each of them. Thus, we are able to fast and cost-efficiently optimize the needed  
 307 electrode for various sample geometries and particle types.

308 Second, for example, for the verification it is however required to judge the actually implanted  
309 ion density. Thus, we developed an optical measurement method to determine non-destructively  
310 the local ratio of sp<sup>2</sup> hybridized carbon atoms from which the degree of modification can be  
311 deduced. It is based on a reflectivity measurement via an optical fibre to ensure flexibility even  
312 for complex-shaped surfaces.

313 Combining both approaches, we demonstrate, by way of example, the optimization of the DLC  
314 modification of an UHMWPE joint inlay. We show that the surface modification of such an  
315 implant can be achieved by using either a combination of a mesh and a cylinder on top or by  
316 using a spherical electrode. Both setups lead to relatively homogeneous surface treatment,  
317 whereas the application of the spherical electrode leads to a slightly higher homogeneity.

318 A promising approach is the combination of our optical setup with a robotic arm which enables  
319 an automation of the measurement process and improves the results by ensuring a constant  
320 distance between the optical head and the surface of the sample. Using LEDs with various  
321 wavelengths to increase the sensitivity according to the fluence range, it is thus conceivable to  
322 apply this method in non-destructive quality assurance in the industrial environment.

323 In summary, we here deliver two useful tools for the DLC transformation of non-planar and  
324 insulating UHMWPE parts like joint replacement components.

325

## 326 **Disclosures**

327 The authors have no financial conflicts of interest.

328

## 329 **Acknowledgments**

330 The authors thank the “Deutsche Forschungsgemeinschaft (DFG)” for the financial support of  
331 this work under the contract “Erkenntnistransferprojekt Antibakterielle und abriebarme  
332 Beschichtung von Gleitflächen in orthopädischen Implantaten”. Moreover, the authors thank  
333 Matthias Weiß and Malina Reitemeyer for technical assistance.

335 **References**

- 336 1. Statistisches Bundesamt (Destatis). Die 20 häufigsten Operationen: Vollstationär behandelte Patientinnen  
337 und Patienten in Krankenhäusern 2016; 2017.
- 338 2. Statistisches Bundesamt (Destatis). Bevölkerung Deutschlands bis 2060: 13. koordinierte  
339 Bevölkerungsvorausberechnung; 2015.
- 340 3. Böhm K, Tesch-Römer C, Ziese T, editors. Gesundheit und Krankheit im Alter. Berlin: Robert Koch-Inst;  
341 2009. (Beiträge zur Gesundheitsberichterstattung des Bundes). ger.
- 342 4. Bleß H-H, Kip M. Weißbuch Gelenkersatz. Berlin, Heidelberg: Springer Berlin Heidelberg; 2017.
- 343 5. Abu-Amer Y, Darwech I, Clohisy JC. Aseptic loosening of total joint replacements: Mechanisms  
344 underlying osteolysis and potential therapies. *Arthritis Res Ther.* 2007;9 Suppl 1S6. doi:10.1186/ar2170
- 345 6. Kaddick C, Catelas I, Pennekamp PH, Wimmer MA. Verschleiss und aseptische Prothesenlockerung:  
346 Eine Bestandsaufnahme [Implant wear and aseptic loosening. An overview]. *Der Orthopäde.*  
347 2009;38(8):690–7. ger. doi:10.1007/s00132-009-1431-9
- 348 7. Sundfeldt M, Carlsson LV, Johansson CB, Thomsen P, Gretzer C. Aseptic loosening, not only a question  
349 of wear: A review of different theories. *Acta Orthop.* 2006;77(2):177–97.  
350 doi:10.1080/17453670610045902
- 351 8. Semlitsch, M., Lehmann, M., Weber, H., Doerre, E., & Willert, H. G. New prospects for a prolonged  
352 functional life-span of artificial hip joints by using the material combination polyethylene/aluminium  
353 oxide ceramic/metal. *Journal of Biomedical Materials Research Part A.* 1977;11(4).
- 354 9. Anne Thomson L, Law FC, Rushton N, Franks J. Biocompatibility of diamond-like carbon coating.  
355 *Biomaterials.* 1991;12(1):37–40. doi:10.1016/0142-9612(91)90129-X
- 356 10. Robertson J. Diamond-like amorphous carbon. *Materials Science and Engineering: R: Reports.*  
357 2002;37(4-6):129–281. doi:10.1016/S0927-796X(02)00005-0
- 358 11. Hauert R. An overview on the tribological behavior of diamond-like carbon in technical and medical  
359 applications. *Tribology International.* 2004;37(11-12):991–1003. doi:10.1016/j.triboint.2004.07.017
- 360 12. Grill A. Diamond-like carbon: State of the art. *Diamond and Related Materials.* 1999;8(2-5):428–34.  
361 doi:10.1016/S0925-9635(98)00262-3
- 362 13. Fedosenko G, Schwabedissen A, Engemann J, Braca E, Valentini L, Kenny JM. Pulsed PECVD  
363 deposition of diamond-like carbon films. *Diamond and Related Materials.* 2002;11(3-6):1047–52.  
364 doi:10.1016/S0925-9635(01)00612-4
- 365 14. Unger E. Die Erzeugung dünner Schichten. Das PECVD-Verfahren: Gasphasenabscheidung in einem  
366 Plasma. *Chemie in unserer Zeit.* 1991;25(3):148–58. doi:10.1002/ciuz.19910250306
- 367 15. Bonelli M, Ferrari AC, Fioravanti A, Li Bassi A, Miotello A, Ossi PM. Structure and mechanical  
368 properties of low stress tetrahedral amorphous carbon films prepared by pulsed laser deposition. *Eur.*  
369 *Phys. J. B.* 2002;25(3):269–80. doi:10.1140/epjb/e20020031
- 370 16. Chowdhury S, Laugier MT, Rahman IZ. Characterization of DLC coatings deposited by rf magnetron  
371 sputtering. *Journal of Materials Processing Technology.* 2004;153-154804–10.  
372 doi:10.1016/j.jmatprotec.2004.04.265
- 373 17. Pappas DL, Saenger KL, Bruley J, Krakow W, Cuomo JJ, Gu T, Collins RW. Pulsed laser deposition of  
374 diamond-like carbon films. *Journal of Applied Physics.* 1992;71(11):5675–84. doi:10.1063/1.350501
- 375 18. Logothetidis S. Hydrogen-free amorphous carbon films approaching diamond prepared by magnetron  
376 sputtering. *Appl. Phys. Lett.* 1996;69(2):158–60. doi:10.1063/1.116906
- 377 19. Calcagno L, Compagnini G, Foti G. Structural modification of polymer films by ion irradiation. *Nuclear*  
378 *Instruments and Methods in Physics Research Section B: Beam Interactions with Materials and Atoms.*  
379 1992;65(1-4):413–22. doi:10.1016/0168-583X(92)95077-5
- 380 20. Schwarz FP, Hauser-Gerspach I, Waltimo T, Stritzker B. Antibacterial properties of silver containing  
381 diamond like carbon coatings produced by ion induced polymer densification. *Surface and Coatings*  
382 *Technology.* 2011;205(20):4850–4. doi:10.1016/j.surfcoat.2011.04.078
- 383 21. Schwarz F, Thorwarth G, Stritzker B. Synthesis of silver and copper nanoparticle containing a-C: Hby ion  
384 irradiation of polymers. *Solid State Sciences.* 2009;11(10):1819–23.  
385 doi:10.1016/j.solidstatesciences.2009.05.012
- 386 22. Buchegger S, Schuster N, Stritzker B, Wixforth A, Westerhausen C. Multilayer diamond-like amorphous  
387 carbon coatings produced by ion irradiation of polymer films. *Surface and Coatings Technology.*  
388 2017;32742–7. doi:10.1016/j.surfcoat.2017.08.010
- 389 23. Hauert R. A review of modified DLC coatings for biological applications. *Diamond and Related*  
390 *Materials.* 2003;12(3-7):583–9. doi:10.1016/S0925-9635(03)00081-5

- 391 24. Conrad JR, Radtke JL, Dodd RA, Worzala FJ, Tran NC. Plasma source ion-implantation technique for  
392 surface modification of materials. *Journal of Applied Physics*. 1987;62(11):4591–6.  
393 doi:10.1063/1.339055
- 394 25. Micheli BR, Wannomae KK, Lozynsky AJ, Christensen SD, Muratoglu OK. Knee simulator wear of  
395 vitamin E stabilized irradiated ultrahigh molecular weight polyethylene. *J Arthroplasty*. 2012;27(1):95–  
396 104. doi:10.1016/j.arth.2011.03.006
- 397 26. Aesculap Orthopaedics. Aesculap® Vitelene® Brochure O44301: Aesculap AG.
- 398 27. Quadrant MediTECH®. Data Sheet Chirulen® 1020-E; 21.01.2014.
- 399 28. Hartwig A. Umwandlung von ultrahochmolekularem Polyethylen in diamantähnlichen Kohlenstoff für  
400 den medizinischen Einsatz [Diploma Thesis]. Augsburg. 84 p. ger.
- 401 29. Meschede D. *Gerthsen Physik*. 24th ed. Berlin: Springer; 2010. (Springer-Lehrbuch). ger.
- 402 30. Prawer S, Nugent KW, Lifshitz Y, Lempert GD, Grossman E, Kulik J, Avigal I, Kalish R. Systematic  
403 variation of the Raman spectra of DLC films as a function of sp<sup>2</sup>: Sp<sup>3</sup> composition. *Diamond and Related*  
404 *Materials*. 1996;5(3-5):433–8. doi:10.1016/0925-9635(95)00363-0
- 405 31. Schwarz-Selinger T, Keudell A v., Jacob W. Plasma chemical vapor deposition of hydrocarbon films:  
406 The influence of hydrocarbon source gas on the film properties. *Journal of Applied Physics*.  
407 1999;86(7):3988–96. doi:10.1063/1.371318
- 408 32. Dowling DP, Donnelly K, Monclus M, McGuinness M. The use of refractive index as a measure of  
409 diamond-like carbon film quality. *Diamond and Related Materials*. 1998;7(2-5):432–4.  
410 doi:10.1016/S0925-9635(97)00233-1
- 411 33. Lifshitz Y. Diamond-like carbon — present status. *Diamond and Related Materials*. 1999;8(8-9):1659–  
412 76. doi:10.1016/S0925-9635(99)00087-4
- 413 34. Mednikarov B, Spasov G, Babeva T, Pirov J, Sahatchieva M, Popova C, Kulischa W. Optical properties  
414 of diamond-like carbon and nanocrystalline diamond films. *Journal of Optoelectronics and Advanced*  
415 *Materials*. 2005;7(3):1407–13.
- 416 35. Rangel EC, Cruz NCd, Kayama ME, Rangel RCC, Marins N, Durrant SF. Optical and Electrical  
417 Properties of Polymerizing Plasmas and Their Correlation with DLC Film Properties. *Plasmas and*  
418 *Polymers*. 2004;9(1):1–22. doi:10.1023/B:PAPO.0000039813.33634.c6
- 419
- 420

421 **Supporting Information: Optimizing lateral homogeneity of ion-induced**  
422 **surface modifications of non-planar dielectric polyethylene components**  
423 **employing ion fluence simulations and optical measurements of the sp<sup>2</sup>-**  
424 **dependent reflectivity**

425  
426 Jochen Taiber<sup>1</sup>, Sascha Buchegger<sup>1</sup>, Bernd Stritzker<sup>1</sup>, Achim Wixforth<sup>1,2,3</sup>, and Christoph  
427 Westerhausen<sup>1,2,3</sup>  
428

429 <sup>1</sup> Chair for Experimental Physics 1, University of Augsburg, Augsburg 86159, Germany

430 <sup>2</sup> Center for NanoScience (CeNS), Ludwig-Maximilians-Universität Munich, 80799  
431 Munich, Germany

432 <sup>3</sup> Augsburg Center for Innovative Technologies (ACIT), Augsburg 86159, Germany

433 \* Correspondence: christoph.westerhausen@gmail.com; Tel.: +49-821-598-3311  
434

435

436

437

438

439

440

441

442

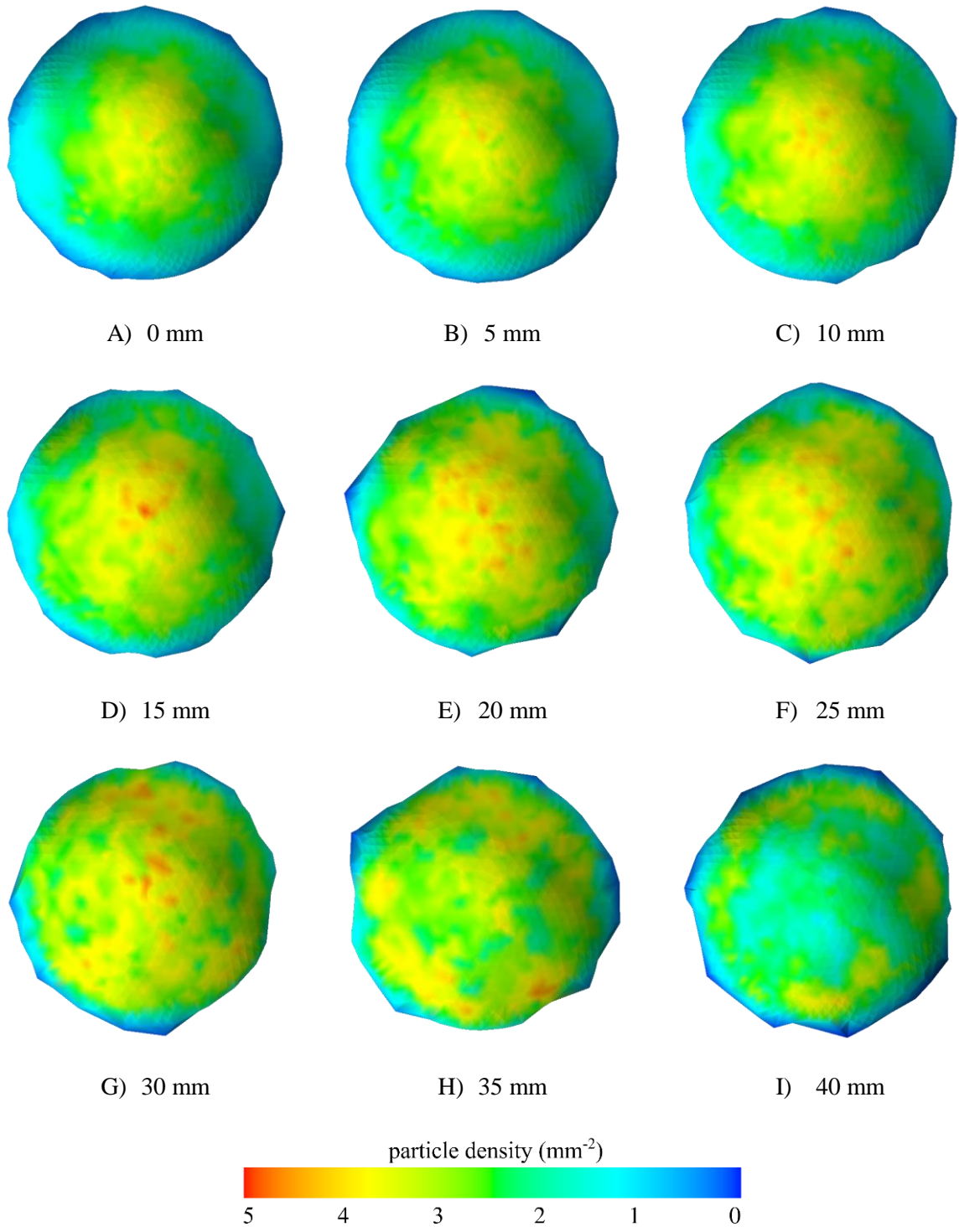
443

444

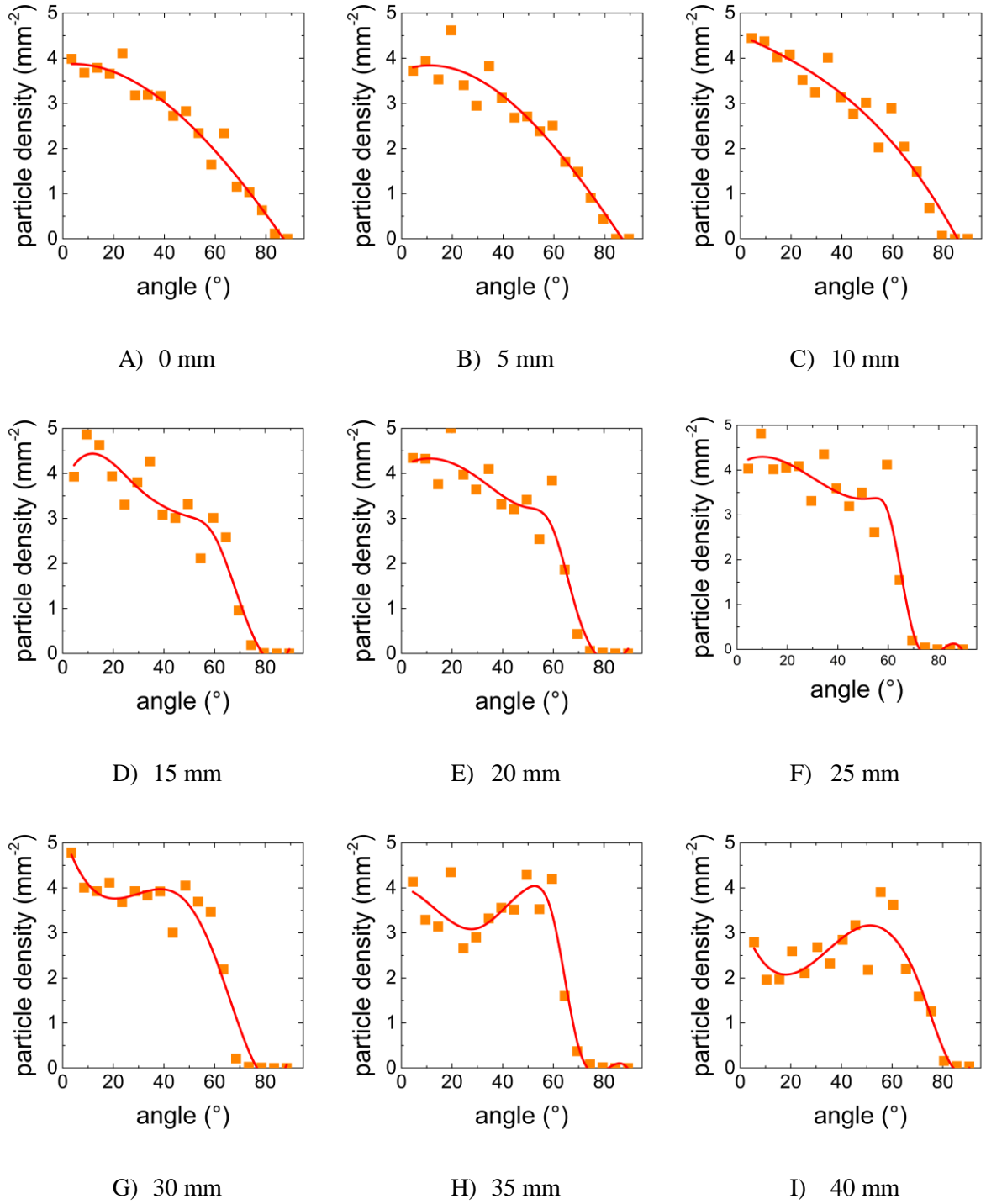
445

446

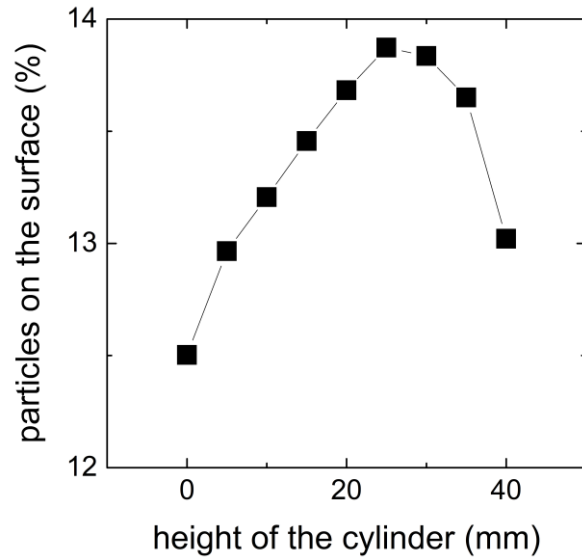
447



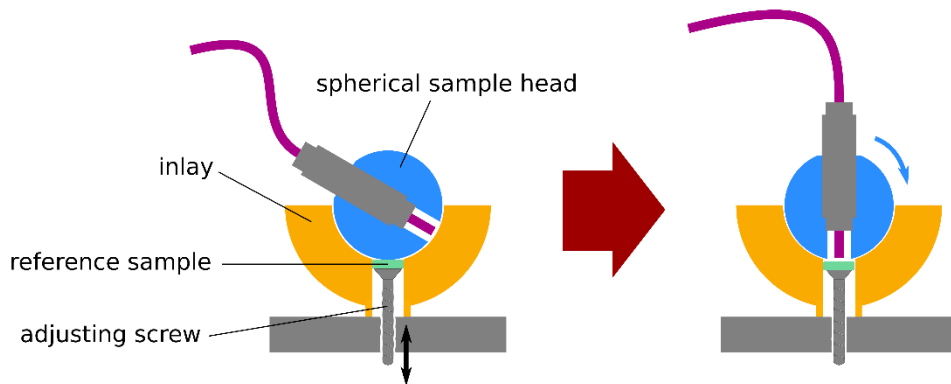
448 *FIG S7: Simulated particle density on the sample's surface using hollow cylinders with different heights (local particle density*  
 449 *of the implanted ions represented by colour scale).*  
 450



451 *FIG S2: Simulated particle density on the sample's surface depending on the position using hollow cylinders with different*  
 452 *heights: if no cylinder is used (0 mm case), the radial decrease is clearly visible. With increasing height of the cylinder, the*  
 453 *"plateau" is getting broader and flatter until a height of 30 mm. Above that value, shadowing occurs.*  
 454



455 *FIG S3: Share of the particles ending on the inner surface of the inlay (compared to the total number of accelerated particles)*  
 456 *depending on the height of the attached hollow cylinder. Above 30 mm cylinder height, shadowing occurs which is responsible*  
 457 *for the decrease in the particle number.*  
 458



459 *FIG S4: Calibration apparatus using reference samples with known fluence: Each sample can be moved up until it touches the*  
 460 *sample head. By turning the head, a reflectivity measurement can be performed ensuring a fixed distance between the optical*  
 461 *fibre and the sample's surface. The result is a calibration curve which is utilized for the conversion of the measurement data*  
 462 *into fluence values.*  
 463